

October 12, 1997

## **SOFT X-RAY PRODUCTION IN SPARK DISCHARGES IN HYDROGEN, NITROGEN, AIR, ARGON, AND XENON GASES**

J. Va'vra  
Stanford Linear Accelerator Center, Stanford University,  
Stanford, CA 94309, U.S.A.

J. A. Maly  
Applied Science Consultants  
5819 Ettersberg Dr., San Jose, CA 95123, U.S.A.

P. M. Va'vra  
67 Pine Lane, Los Altos, CA 94022, U.S.A.

### **ABSTRACT**

We describe a generator of soft X-rays of energy between 2 and 10 keV by sparking in hydrogen, air, nitrogen, argon, and xenon gases at low pressure with a sparking voltage as low as ~0.8 kV, which can be used as a simple monitor of the gaseous detectors. The X-ray production mechanism is also discussed, including the possibility of a new process.

(Submitted to Nuclear Instruments and Methods)

### **1. INTRODUCTION**

We present a simple X-ray generator which can be used to monitor drift chambers. The generator uses a spark gap operating at low pressure, with a thin window and very low voltages between 0.8 and 2.5 kV to create X-rays between 2 and 10 keV.

To create the X-rays by sparking in low pressure is not new. Less known is the fact that one can create the X-ray energies, which are larger than the sparking voltage. This seemingly surprising effect is semi-qualitatively explained in the literature by the so called "pinch" effect [1-4], which is known to occur during very large low inductance sparks, operating typically with initial charging voltages of 10-60kV, charging capacitance of 10-20 $\mu$ F, low inductance of ~100 nH, stored energies of 1-3 kJ/pulse, and peak spark currents of 100-200kA [1]. The pinch effect has been demonstrated experimentally using pin hole photography, which indicates a formation of point-like (plasma points) regions within the plasma [2]. A generally accepted explanation of the pinch effect is based on the radiation collapse model [1]. During the pinch effect, one observes a formation of dips in spark current, which in turn creates large local voltages [1]. The voltage across the sparking gap can exceed the supply voltage by a factor of 2-3 [3], and thus, the X-ray energies can exceed the sparking voltage. The current dips are correlated with the appearance of plasma points, which principally emit X-ray lines of the anode material; radiation from the cathode material is weak [1]. The X-ray production shows a strong angular anisotropy [4]. The sparks in the above tests are so

large that the electrodes wear out quickly. Indeed, the spectral investigations reveal emission from heavily ionized atoms, which are present in the electrode material [2].

In our tests, we tried to set the smallest possible sparks that are still consistent with the X-ray production, i.e., we tried to operate at the opposite end of the spark's stored energies, as mentioned above. The sparking voltage varied between 0.8 and 2.1kV, the charging capacitance was 75nF, inductance was  $\sim 1000\text{nH}$ , stored energy was 0.024-0.17J/pulse, the peak spark currents were 0.2-0.5kA, and the total spark charge was between  $4 \times 10^{14}$  and  $10^{15}$  electrons/spark. The observed X-ray energies were between 2 and 10 keV, even at the lowest sparking voltage of  $\sim 0.8\text{kV}$  (depending on the gas), and followed an exponential distribution falling towards larger X-ray energies. The maximum observed X-ray energy ( $\sim 10\text{keV}$ ), generated at the lowest voltage ( $\sim 0.8\text{kV}$ ), is above K-shell energy of typical gases we used in our tests, and materials used in our spark electrodes (see Table 1 and Chapter 4). The X-ray production persists even for the carbon electrodes which have the smallest K-shell energy (0.284keV); this would appear to eliminate a theory that the electrode atoms are responsible for the X-ray production. Furthermore, we have evidence that the production threshold and the X-ray rate are dependent on the gas choice in the sparking vessel. We have measured the  $I(t)$ ,  $V(t)$ , and  $dI/dt(t)$  curves and have confirmed that the X-rays are produced during the largest swing in the  $dI/dt(t)$  curve corresponding to a dip in the current  $I(t)$ . This would appear to be consistent with the earlier mentioned pinch effect mechanism. The sparks in our tests are relatively large by a typical standard, however, compared to the spark energies used in Refs.1-4, they are considerably smaller, by at least a factor of  $\sim 4 \times 10^4$  (at  $\sim 0.8\text{kV}$ ). If our results are due to the pinch effect, we are then observing the pinch effect phenomenon at the smallest spark energy reported so far in the literature, i.e., we are investigating its threshold behavior.

However, we have some doubts that the pinch effect is really understood quantitatively. The sparking phenomenon is an extremely complex process if we insist on a real quantitative evaluation of its dynamics. Its understanding is not yet at a level of that of the electron transport at low drift electric fields or small avalanches, which can be solved reasonably accurately using the three-dimensional Monte Carlo simulation [5] [the computer program follows the electrons and ions in small steps (fraction of a ps) and evaluates electrostatic forces, position and velocities of each electron and ion, and probability of various physics processes using the electron-molecule scattering cross-sections]. It is not possible to do this for sparks having large number of electrons involved in the pinch effect at this time, not only because of the computational difficulties but also because one does not necessarily know details of all physics processes involved. For example, in Chapter 4 we mention one additional possible mechanism which may have been neglected in the theory of the pinch effect, and may contribute to the X-ray production in our tests.

One practical benefit of running small spark energy is that the sparking electrodes do not wear out quickly and the device is suited for long-term investigations. The spark electromagnetic noise requires careful shielding for fast detectors. For drift chambers with a long drift, one can be easily protected by a drift time delay of about 1-2  $\mu$ s. The X-rays were monitored at 90° in respect to the spark axis during all tests in this paper. An initial approximate observation indicates that they may be isotropic, although this is yet to be confirmed by a larger test detecting X-rays over a larger solid angle.

## 2. EXPERIMENTAL SETUP

### 2.1. Description of X-ray producing apparatus

Figure 1 shows schematically the spark producing apparatus. It uses a spark gap with a 1 mm gap between the points, which is placed in a small brass vessel equipped with a thin window to allow low energy X-rays to penetrate (in final tests we also used carbon electrodes in a specially prepared spark gap). The window opening is  $\sim 1.27$  cm diameter and its material is either 12.7  $\mu$ m stainless steel (sealed by a conducting epoxy), or 50  $\mu$ m Mylar foil. The sparking vessel is connected to a vacuum pump from one side, and to a gas bottle from another side. The gas pressure is controlled by a small needle valve throttling the gas flow while pumping. The pressure is monitored by a thermocouple gauge with an accuracy of a few microns (1  $\mu$  =  $10^{-3}$  Torr). The pump was capable of reaching a pressure (p) of 10-20  $\mu$ .

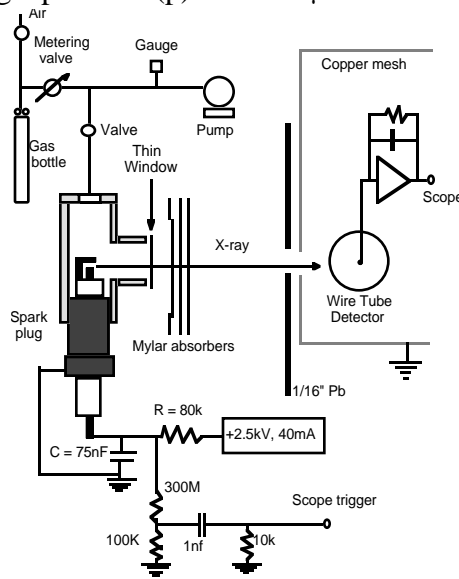


**Fig. 1.** Our experimental setup for sparking in gases at low pressure. It uses a spark plug with a 1 mm gap, operating as a relaxation oscillator.

The operating parameters of the spark gap were tuned to maximize the X-ray production; this occurs in a relatively narrow window of the parameter space. The spark gap operates at low

pressure between 0.2 and 1Torr, depending on the gas choice. It operates as a relaxation oscillator with a charging resistor  $R = 80\text{k}\Omega$  and a charging capacitor  $C = 75\text{nF}$ . Because of excessive heating, the charging resistor  $R$  is made with an equivalent circuit involving six pairs of  $\sim 27\text{k}\Omega$ , 10W resistors; it is necessary to cool them with a small fan. The high voltage power supply, capable of delivering up to 40 mA DC current, operates at +2.5kVDC voltage. The sparking voltage ( $V_{\text{spark}}$ ) varies between 0.8 and 2.1kV, which corresponds to a spark energy ( $\frac{1}{2}CV_{\text{spark}}^2$ ) between 0.024 and 0.17J/pulse, and a spark charge ( $CV_{\text{spark}}$ ) between  $4 \times 10^{14}$  and  $10^{15}$  electrons/spark. The spark repetition period ( $T$ ) is set typically between 5 and 20ms by the choice of gas pressure, which corresponds to sparking rates between 50 and 200Hz.

## 2.2. Spark voltage monitoring

First, we calibrated the DC power supply output with a precision voltage divider and a digital voltmeter. This resulted in a small  $\sim 0.6\%$  correction. Second, we calibrated a spark voltage  $V_{\text{spark}}$  relative to a spark period  $T$  using a special voltage divider, as shown in Fig.2a. To monitor the varying voltage with a voltage divider, it is necessary to compensate the resistors for their parasitic capacitance. This was done by measuring a parasitic capacitance of the  $300\text{M}\Omega$  resistor in Fig.2a, and then empirically tuning the  $80\text{nF}$  capacitor to minimize an undershoot in the monitored voltage of Fig.2b. The monitored voltage of Fig.2b was used to determine a correlation between the sparking voltage  $V_{\text{spark}}$  and a sparking period  $T$  of the oscillator. By measuring the sparking period  $T$ , one can uniquely determine the sparking voltage  $V_{\text{spark}}$ , which is shown in Fig.2c. Finally, we have also used a spark gap<sup>1</sup> CG3-1.5 to calibrate  $V_{\text{spark}}$ . Its sparking voltage was selected to be 1.4kV. For  $V_{\text{spark}} < 1.4\text{kV}$ , the spark gap did not fire. This was a simple way to confirm that our calibration is correct, and that there is no fast transient exceeding  $V_{\text{spark}}$ .

The relaxation oscillator has the following feature: for a given spark gap distance  $d$ , gas pressure  $p$  and gas choice, the sparking voltage  $V_{\text{spark}}$  is determined according to Paschen's law, which says that  $V_{\text{spark}}$  is a function of  $pd$ . We operated in a region of the law where increasing the pressure reduces the sparking voltage, which in turn reduces the sparking period  $T$ .

During the experiment, we would typically monitor the sparking period, which is easy to measure, and use the calibration curve of Fig.2c to obtain the corresponding sparking voltage. Depending on the choice of the gas pressure in a given gas, we would typically select the sparking voltage  $V_{\text{spark}}$  between 0.8 and 2.1kV during this experiment, while running the high voltage power supply always at a constant value of +2.5kV. We used the scope triggering circuit, described in Fig.1, to determine the sparking frequency  $T$ .

---

<sup>1</sup> Made by General Instrument Co., Chicago, IL 60645, U.S.A.

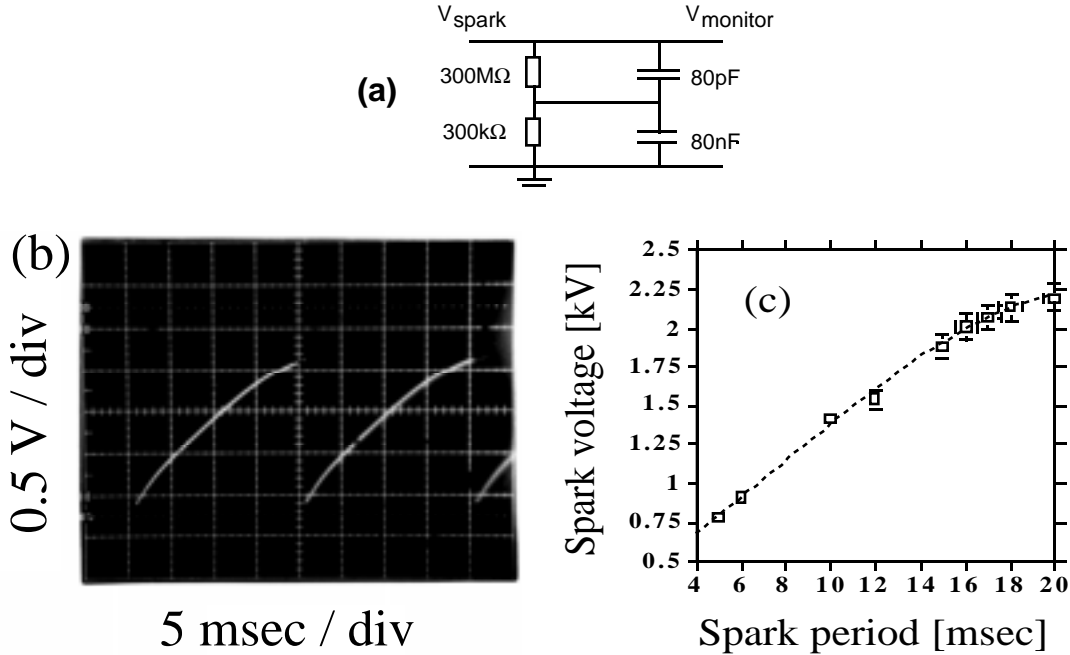


**Fig. 2.** We used a special voltage divider (a), equipped with a capacitive correction, to determine a sparking voltage  $V_{\text{spark}}$  and a sparking period  $T$  (b). A calibration curve correlating the sparking voltage  $V_{\text{spark}}$  and the park period  $T$  is shown in (c).

### 2.3. X-ray detectors

We have used four types of X-ray detectors during this test: a Geiger detector TBM-3S<sup>2</sup>, a single wire proportional tube detector, a long drift detector, and the YAP scintillator<sup>3</sup> coupled to the XP2230 photomultiplier<sup>4</sup>. The most prominent systematic effect was the spark noise generated by the spark gap located very close to the detector. To limit its influence, we have constructed a large copper mesh Faraday cage around the detector, the connecting cables were placed in the grounded copper pipes, and the spark gap vessel and its high voltage connection was well grounded. The signal detection in the wire tube detector and the YAP scintillator occurs during the largest spark noise, and therefore, it was necessary to place them in the second local coaxial shield. The easiest way to eliminate the spark noise was with the long drift detector because in this particular geometry one can easily separate the spark noise from the X-ray signal by a choice of a suitable electric drift field. In all cases, it was easy to verify that we indeed detect the X-rays by placing an absorber between the spark plug vessel and the detector window.

<sup>2</sup> Made by Technical Associates, Canoga Park, CA 91303, U.S.A

<sup>3</sup> YAP stands for  $\text{YAlO}_3:\text{Ce}$ ; density  $5.37\text{ g/cm}^3$ , peak emission at 370nm, typically 3-4 p.e./keV.

<sup>4</sup> Made by Amperex, North American Philips Co.

The Geiger detector TBM-3S is a commercially made battery operated detector equipped with a thin Mylar window of a  $1.5 \text{ mg/cm}^2$  thickness and 5 cm diameter. It is filled with halogen gas.

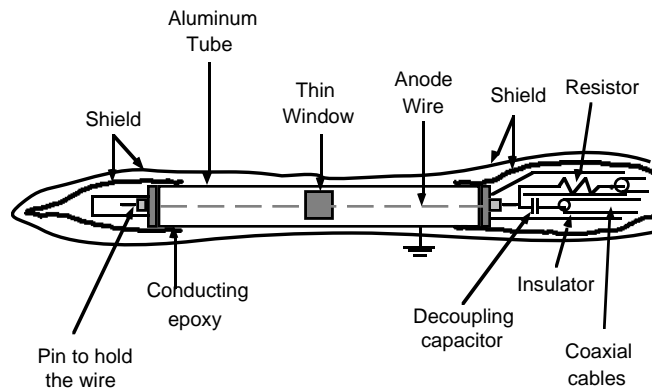


**Fig. 3.** Geometry of the single wire proportional tube detector including its spark noise shield.

Figure 3 shows the geometry of the wire tube detector. The gold plated tungsten anode wire diameter is  $38 \mu\text{m}$ . The aluminum tube has 10 mm i.d. with a 1 mm wall thickness. The tube has a 10 mm x 10 mm opening in the center, which is covered with a  $30 \mu\text{m}$  thick aluminized Mylar foil. The foil is connected electrically to the tube wall with conducting epoxy and sealed with a DP-190 epoxy. The detector is operating with a 95% Ar+5%  $\text{CH}_4$  gas mixture at 1 atm pressure. This choice was primarily motivated by its nonflammability.

Figure 4 shows the geometry of the long drift wire detector. The drift cell is made of two sections: a drift region made of equally spaced stainless steel rings and a gain region containing  $20 \mu\text{m}$  gold plated anode wires surrounded by a nickel plated cathode. The drift field is defined by the potentials  $V_1$  and  $V_2$ . The resistor chain provides voltages to the individual stainless steel rings. The value of each resistor is  $10\text{M}\Omega$ . The drift region has a cylindrical shape with 2.5 cm i.d. and 12 cm long active volume. The entrance window into the long drift detector is made of  $\sim 13 \mu\text{m}$  thick aluminized Mylar foil. The gas gain is controlled by the cathode voltage  $V_C$ . All anode wires are connected together to a single amplifier. The detector also operates with a 95% Ar+5%  $\text{CH}_4$  gas mixture at 1 atm pressure. To be insensitive to a spark noise, we would typically choose a drift field of only  $\sim 8\text{-}10\text{V/cm}$  corresponding to a very low electron drift velocity of  $\sim 5\text{mm}/\mu\text{s}$ . Typically, with this detector, the spark noise would appear only in the first 1-2  $\mu\text{s}$  after the scope trigger, followed by a perfect noise-free period. We would then observe events of interest between 3 and 25  $\mu\text{s}$  after the scope trigger.

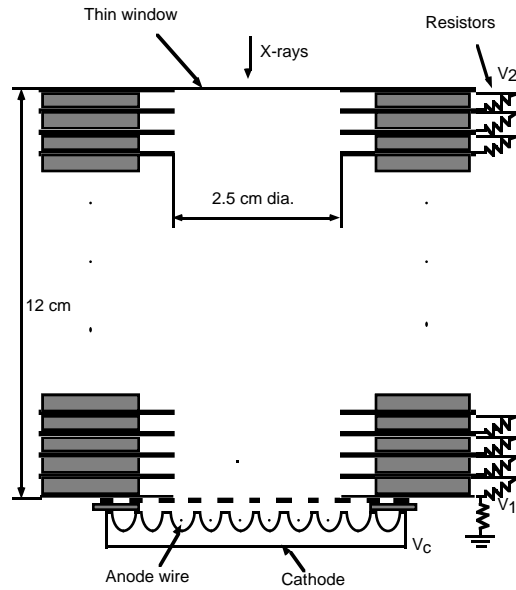


**Fig. 4.** Geometry of the long drift detector.

The YAP scintillator was a cube (1cm x 1cm x 1cm) coupled to a XP2230 PM tube with a UV coupling grease. A good light collection was ensured by covering the sides of the scintillator with Teflon tape; the light leak was stopped with two layers of black paper tape. Because we used an amplifier with a large gain ( $\sim 15\text{mV/pC}$ ), the photomultiplier tube (PM) operated at a very low voltage of  $-1.4\text{kV}$ . The main reason to use this detector was to investigate the high energy end (tens of keV) of the pulse height spectrum, where the gaseous detectors start losing efficiency.

#### **2.4. Electronics used in the test**

The long drift detector was used to measure the multiplicity of the X-ray bursts. Its amplifier was a battery operated charge sensitive amplifier with a gain of  $\sim 15\text{mV/pC}$ , a shaping time of  $\sim 65\text{ns}$ , and  $\sigma_{\text{noise}} \sim 2000 e^-$ . This sensitivity is enough to be able to detect even single electrons arriving on the wire, assuming that the gas gain is in the range of  $10^5$ . A conversion of a 3-10keV X-ray generates a much larger signal, equivalent to several hundred electrons.

The wire tube detector measured the X-ray pulse height spectra using two methods: (a) peak sensing method using a LeCroy TRA100 amplifier with a gain of  $\sim 50\text{mV/pC}$  and a shaping time of  $\sim 20\mu\text{s}$ , together with a digital oscilloscope (reading individual pulses manually), (b) charge sensing method using the battery operated amplifier (see above) with the pulse height analyzer LeCroy QVT 3001 in q-mode operating with an external 400ns long gate (the YAP scintillator detector was also using this method).

## 2.5. Expected X-ray attenuation factors and detection efficiency

Figures 5a and 5b show calculated attenuation curves for various materials and an expected detection efficiency for the tube and long drift wire detectors.

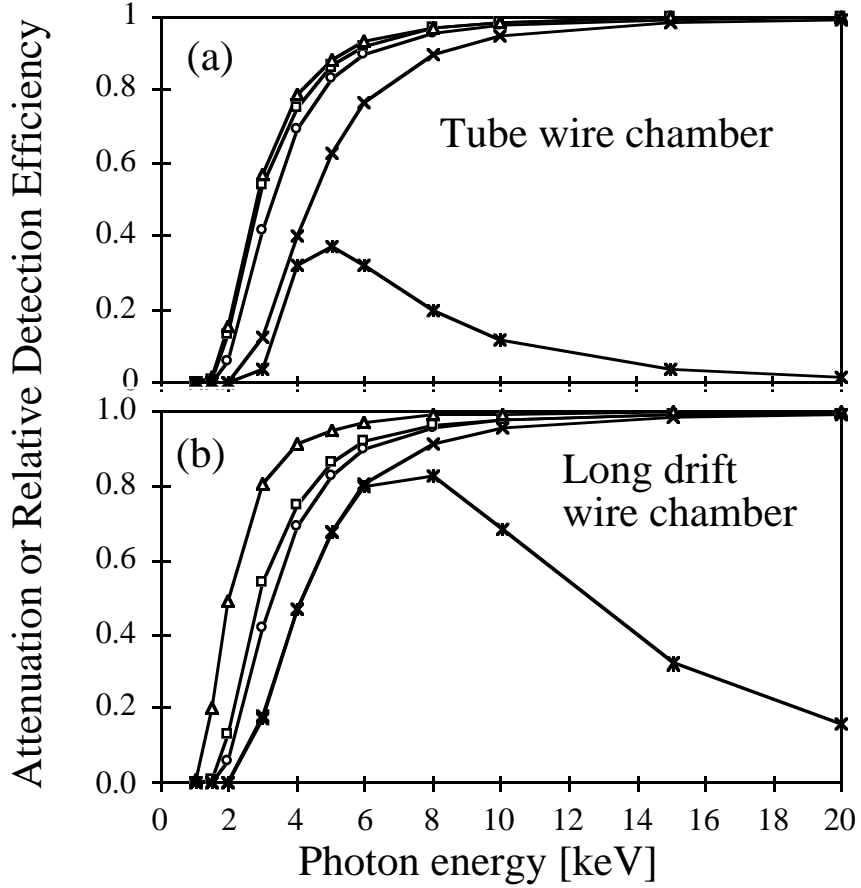


**Fig. 5.** Calculated attenuation  $N/N_0$  curves for various materials in the X-ray path, and expected X-ray detection efficiency for (a) the tube wire chamber and (b) the long drift detector. The attenuation was calculated for 51  $\mu\text{m}$  thick Mylar sparking vessel window (open circles), 3 cm of air (squares), 33  $\mu\text{m}$  (tube) or 12.5  $\mu\text{m}$  (long drift) wire chamber window (triangles), the combined attenuation factor (x) and the final detection efficiency (star).

The attenuation factor is defined as  $\eta(E) = N/N_0 = \exp(-L/L_0)$ , where  $L$  is the X-ray path length and  $L_0$  is the attenuation length calculated from the absorption coefficient in a given material [6]. The X-ray detection efficiency,  $\epsilon(E)$ , defined as a ratio of detected and produced number of X-rays, was calculated as follows:

$$\epsilon(E) = \eta_{\text{mylar}}(E) \eta_{\text{air}}(E) \eta_{\text{window}}(E) (1 - \eta_{\text{gas}}(E)) \quad (1)$$

where  $\eta_{\text{gas}}$  is the attenuation in 95% Ar+5% CH<sub>4</sub> gas mixture, and other factors are the attenuation factors in the materials in the X-ray path. We assume that the wire chamber detection efficiency is

close to 100% for a charge generated by the X-rays. From Fig.5b, one can see that the long drift detector has a good X-ray detection efficiency between 3 and 20keV.

### 3. EXPERIMENTAL RESULTS

We have observed X-ray production with all four types of detectors described in Section 2.3. There are three arguments for this statement: (a) the radiation was not affected by a strong magnet placed between the sparking vessel and the detector, indicating that we are indeed dealing with the X-rays or neutral particles; (b) the range measurements are very consistent with the X-ray production; (c) the response from the gaseous detectors strongly indicates soft X-ray production (pulses are comparable in size and shape to pulses from an  $\text{Fe}^{55}$  X-ray source). The X-rays were monitored at  $90^\circ$  in respect to the spark axis during all tests in this paper.

#### 3.1. Observation of X-ray showers

The most convincing proof of the existence of the X-ray bursts in a single event came from the long drift detector. The long drift detector operating condition was described in Section 2.3. A fraction of the solid angle extended by the sensitive region of the long drift detector in this test was  $\Delta\Omega/\Omega\sim 0.0019$ . Fig.6a shows oscilloscope pictures of the X-ray events, which follow the initial spark noise. The relaxation oscillator was operating in air at  $V_{\text{spark}}\sim 1.45\text{kV}$  and  $p\sim 270\mu$ .

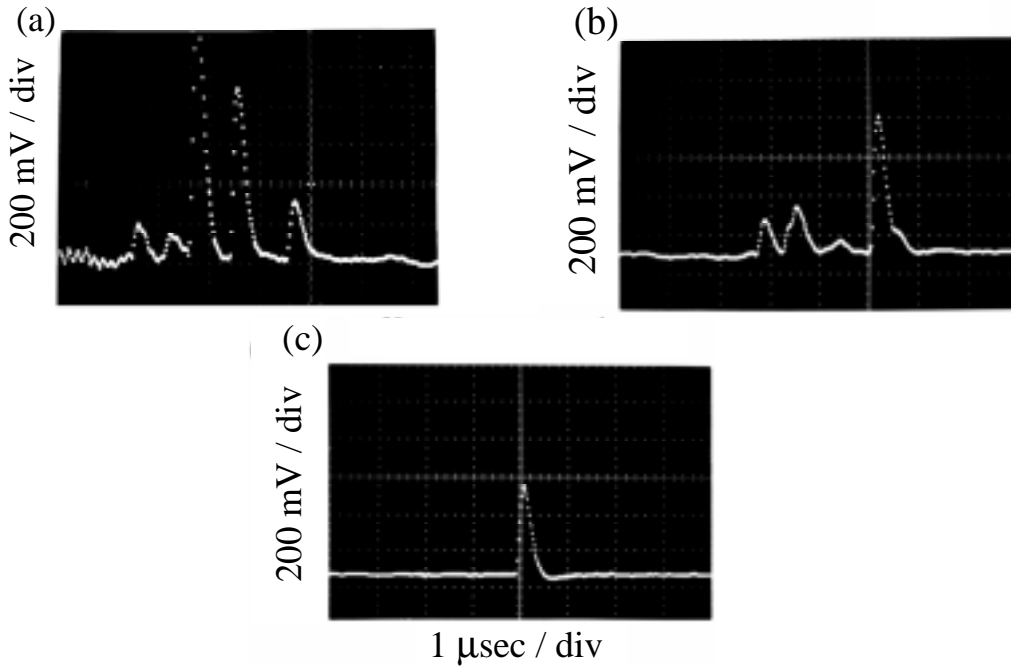


**Fig. 6.** (a) A cluster of X-ray pulses detected in the long drift detector; sparking in air at a sparking voltage  $V_{\text{spark}}\sim 1.45\text{kV}$  and a pressure of  $\sim 270\mu$ ; (b) A cluster of X-ray pulses detected in the long drift detector; sparking in argon at a sparking voltage  $V_{\text{spark}}\sim 2\text{kV}$  and a pressure of  $\sim 170\mu$ ; (c) A calibration pulse from an  $\text{Fe}^{55}$  X-ray source for the same gas gain.

Figure 6b shows similar X-ray production with argon at  $V_{\text{spark}} \sim 2\text{kV}$  and  $p \sim 170\mu$ . For comparison, Fig. 6c shows a typical calibration pulse from the  $\text{Fe}^{55}$  X-ray source. Notice that the X-ray events appear in clusters (Figs. 6a and b). To study the single X-ray events, it is necessary to adjust their flux so that the probability to observe the X-ray pulse per spark was only  $\sim 5\%$ , thus ensuring only a small probability of a pile-up from different events. This is achieved by placing an additional  $178\mu\text{m}$  Mylar absorber in the X-ray path, creating a total Mylar thickness of  $261\mu\text{m}$  between the spark and the sensitive volume of the long drift detector. The sparking vessel is filled with argon, and operates at  $V_{\text{spark}} \sim 2\text{kV}$  and  $p \sim 170\mu$ . The counting of X-ray pulses is done visually using a digital scope. Fig.7 shows a multiplicity distribution of the X-ray pulses per spark, indicating a mean of three. Extrapolating this result to a  $4\pi$ -solid angle and assuming an isotropic distribution, one would expect more than  $3 * (\Omega / \Delta\Omega) \sim 1500$  X-ray pulses.

From a visual observation of scope traces, it appears that the average energy of the X-rays is below  $\sim 10\text{keV}$ . The signal disappears when placing either a  $1.6\text{mm}$  thick lead sheet or even a  $762\mu\text{m}$  thick Mylar sheet in front of the long drift detector (see the next chapter for a quantitative evaluation of average energy).

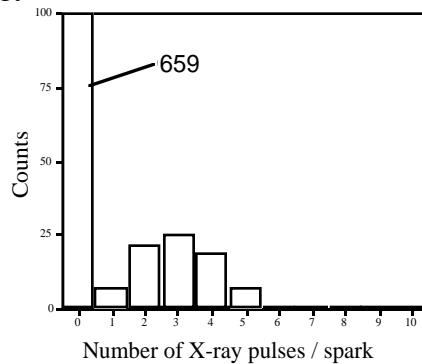


**Fig. 7** An average X-ray multiplicity per spark in argon, sparking voltage  $V_{\text{spark}} \sim 2\text{kV}$  and pressure of  $\sim 170\mu$ .

The X-ray energy was between 3 and  $10\text{keV}$  on average, and probability to observe an X-ray pulse per given spark was kept at only  $\sim 10\%$  to ensure a proper X-ray counting.

### 3.2. Average effective X-ray energy using a range measurement

An advantage of the range measurement is that it is simple and insensitive to any spark noise. We have used Mylar, Kapton, aluminum, and stainless steel absorbers mounted into slide frames. The slides were carefully placed into an X-ray path between the sparking vessel and the detector. Fig. 8a shows a comparison of calculated and measured attenuation curves for the setup using the Geiger counter TBM-3S. The X-rays passed through a  $12.7\mu\text{m}$  thick stainless steel sparking vessel window, 3 cm of air and  $38\mu\text{m}$  of Mylar foil on the counter. The sparking vessel was operating with air at  $V_{\text{spark}} \sim 2.1\text{kV}$  and  $p \sim 240\mu$ . One can see that an average measured effective

energy of X-rays is slightly above 4keV. Fig.8a also shows the measured calibration data using the  $Fe^{55}$  source producing 5.9keV X-rays; it agrees fairly well with the calculation.

Fig.8b shows a comparison of the calculated and measured attenuation curves for the setup using the tube wire detector. In this case, the X-rays passed through a  $12.7\mu\text{m}$  thick stainless steel sparking vessel window, 3 cm of air, and a  $30\mu\text{m}$  thick aluminized Mylar foil of the tube window. The sparking vessel was operating with air at  $V_{\text{spark}}\sim 2.1\text{kV}$  and  $p\sim 240\mu$ . Again, one can see that an average effective energy of X-rays is slightly above 4keV. Fig.8b also shows the calibration data using the  $Fe^{55}$  source producing 5.9keV X-rays. Both methods, one using the Geiger counter and one using the tube wire detector, agree with each other.

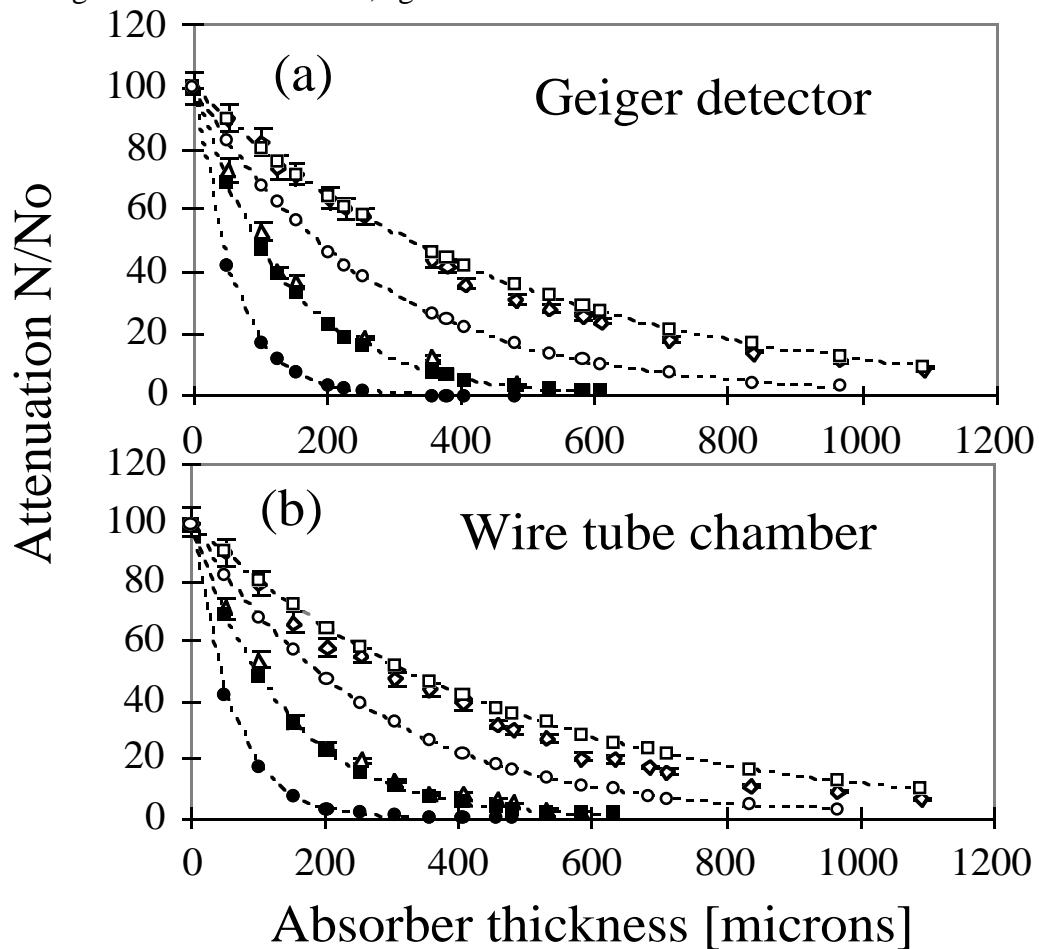


**Fig. 8** (a) A comparison of a range measurement and calculated attenuation curves using the Geiger counter TBM-3S. The sparking data (open triangles) were obtained with air at sparking voltage  $V_{\text{spark}}\sim 2.1\text{kV}$  and pressure of  $240\mu$ , calibration was done using the  $Fe^{55}$  X-ray source (open diamonds), the calculation was done at 6keV (open squares), 5keV (open circles), 4keV (filled squares), and 3keV (filled circles). (b) The same for the tube wire detector; the sparking vessel was operating with air at sparking voltage  $V_{\text{spark}}\sim 2.1\text{kV}$  and pressure of  $240\mu$ .

The spark charge contains approximately  $\sim 10^{15}$  electrons. The question is, what is the probability that one such electron creates an event, containing any number of X-ray pulses. Combining the results from the long drift detector of Sections 3.1, and the tube detector of Section 3.2, we calculate this probability as follows:  $\sim 0.1 * 5 * 10^{-15} = 5 \times 10^{-16}$ , where 0.1 is the probability to observe an X-ray even per spark containing  $10^{15}$  electrons, a factor of 5 comes from the absorption correction caused by the  $262 \mu\text{m}$  Mylar absorber in the X-ray path (see the multiplicity measurement in chapter 3.1), assuming an average X-ray energy  $\sim 4\text{keV}$  - see Fig.8b. To be able to see this phenomenon one needs a very large instantaneous spark current ( $>400\text{A}$ ). For example, one would not see it using electrons from an ordinary  $\beta$ -source.

### **3.3. X-ray energy distribution**

The difficulty to correctly measure the pulse height distribution in this experiment is mainly related to a short duty cycle of the X-ray production, and to a spark noise. The X-rays are produced within  $\sim 150\text{-}200\text{ns}$  time interval (see Section 3.5), and they seem to occur in multiple events (see Section 3.1). To assure that we are dealing predominantly with the single X-ray pulses when measuring the pulse height spectra, we need to limit the probability of a single X-ray pulse per spark to less than 5%. This is achieved by (a) restricting the X-ray flux with a  $\sim 1\text{mm}$  diameter hole in the  $1.5\text{mm}$  thick lead sheet, and (b) by running at the lowest possible sparking voltage. Despite these precautions, there is still a nonzero chance of having two X-ray pulses within the integration gate, and therefore, one should not over-interpret a maximum X-ray energy measured in the test. The maximum observed energy is also affected by a resolution of the detector, which has to be determined by a separate calibration run. The spark noise was reduced by using careful shielding precautions (see Section 2.3), and by running relatively long shaping time of the amplifier, which, however, made it more difficult to resolve doubles.

#### **3.3.1. Wire tube detector with a long integration time constant.**

We use a charge integrating amplifier with a gain of  $\sim 50\text{mV/pC}$  and a shaping time of  $\sim 20 \mu\text{s}$ , and a digital oscilloscope to measure the pulse height spectrum by determining a peak of each pulse. In this way, every pulse contributing to the pulse height spectrum is visually checked. The X-rays pass through a  $51 \mu\text{m}$  thick Mylar window of the sparking vessel,  $3 \text{cm}$  of air and a  $30 \mu\text{m}$  thick aluminized Mylar foil of the wire tube window before there is a detection in the wire tube chamber operating with  $95\% \text{Ar} + 5\% \text{CH}_4$  gas.

Figure 9a shows the uncorrected X-ray pulse height spectra in air, hydrogen, argon, and xenon gases. The spark gap operates at  $V_{\text{spark}} \sim 0.9\text{kV}$  and  $p \sim 310 \mu$  for air, at  $V_{\text{spark}} \sim 1.55\text{kV}$  and  $p \sim 950 \mu$  for hydrogen, at  $V_{\text{spark}} \sim 0.8\text{kV}$  and  $p \sim 240 \mu$  for argon, and at  $V_{\text{spark}} \sim 1.81\text{kV}$  and  $p \sim 135 \mu$  for xenon.

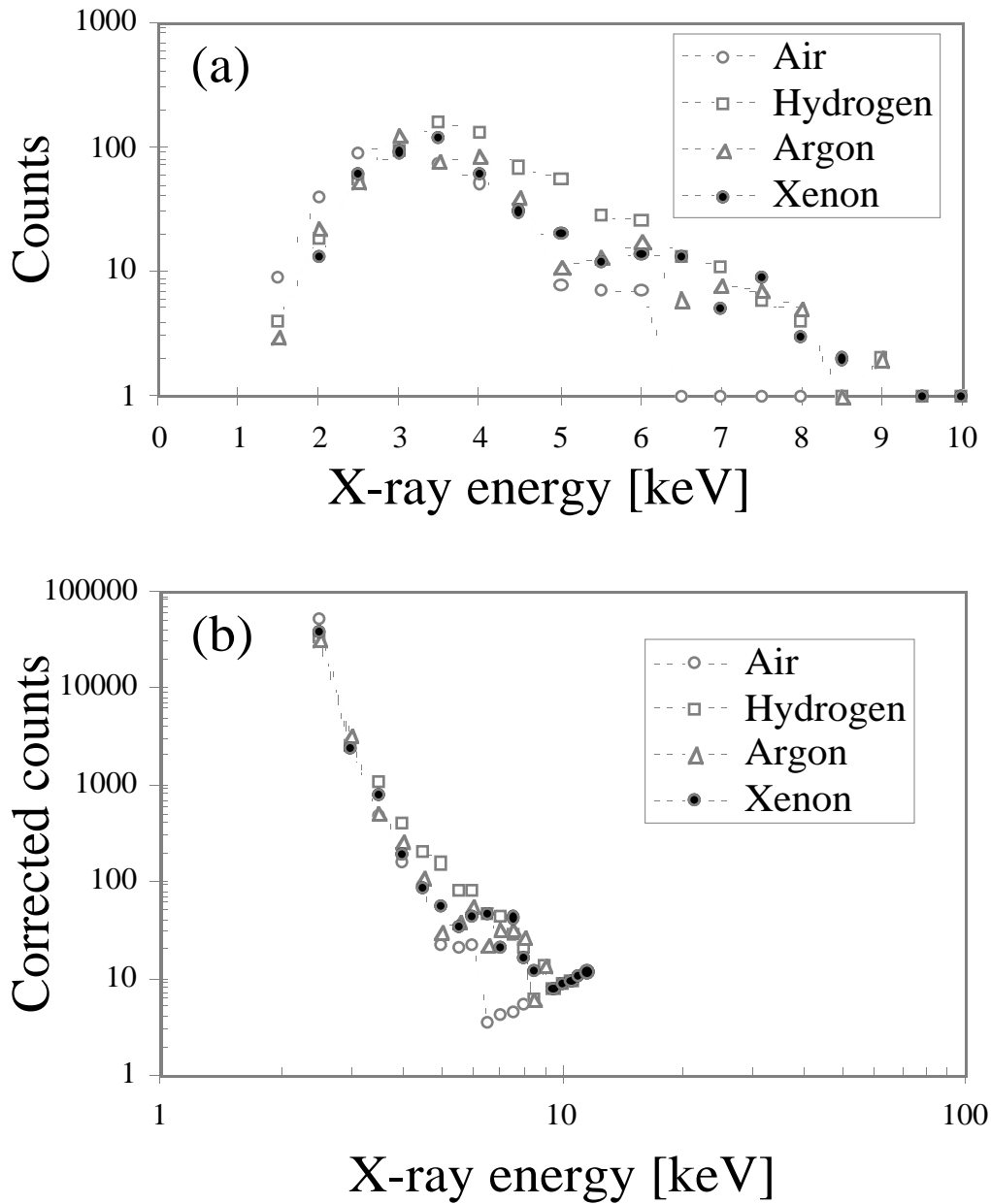


**Fig. 9.** (a) A measured X-ray pulse height spectrum using the wire tube detector while sparking in air at  $\sim 0.9$  kV; hydrogen at  $\sim 1.55$  kV; argon at  $\sim 0.8$  kV; xenon at  $\sim 1.81$  kV. The X-rays pass through the  $51 \mu\text{m}$  Mylar window in the sparking vessel, 3 cm of air, and a  $30 \mu\text{m}$  thick aluminized Mylar foil in the wire tube chamber. The energy scale is calibrated using the  $\text{Fe}^{55}$  source; the resolution  $\sigma/\text{Peak}$  of the wire tube detector is  $\sim 14\%$  at 5.9 keV. (b) The same pulse height spectra as shown in Fig. 9a, but corrected for the attenuation factors in various materials and the wire tube X-ray detection efficiency - see Fig. 5a.

Using the calculated attenuation factors for each absorber in the X-ray path, and using the calculated wire tube detection efficiency based on the energy dependent attenuation factors in each component of the chamber gas (see Eq.1, Ref.6, and Fig.5a), one can correct the measured spectra of Fig.9a and obtain a shape of the primary X-ray spectra at the source. Fig.9b shows the final results for air, hydrogen, argon, and xenon in the sparking vessel. The spectra have the same shape within the experimental errors and they follow a power law distribution.

The scale is calibrated with the  $\text{Fe}^{55}$  radioactive source. The resolution  $\sigma/\text{Peak}$  of the wire tube detector is  $\sim 14\%$  at 5.9 keV.

### **3.3.2. Wire tube detector with a short integration time constant**

In this test, the wire tube detector is coupled to the charge integrating amplifier with a gain of  $\sim 15\text{mV/pC}$  and shaping time of  $\sim 65\text{ns}$ . The pulse height spectrum is measured using the QVT pulse height analyzer operating in the charge integrating mode (q-mode) with an external gate of 400ns long. The shape of the X-ray distribution and the maximum energy observed in argon and xenon are consistent with the results presented in Fig.9a.

### **3.3.3. YAP scintillation detector with a short integration time constant**

In this test, the YAP scintillation detector is coupled to a PM operating at -1.4kV. The PM anode output is amplified by the charge integrating amplifier with a gain of  $\sim 15\text{mV/pC}$  and the shaping time of  $\sim 65\text{ns}$ . As indicated above, the pulse height spectrum is measured using the QVT pulse height analyzer operating in q-mode with a 400ns long external gate.

In this case, we are interested to see if there are some X-rays with much larger energies than  $\sim 10\text{keV}$ . Fig.10a shows the uncorrected X-ray pulse height spectrum in xenon on the logarithmic scale. The spark gap was operating at  $V_{\text{spark}} \sim 1.81\text{kV}$  and  $p \sim 135\mu$ . Fig.10b shows the same spectrum, but in this case the X-rays are blocked with 1.5mm thick lead sheet. As expected, no events are observed above the pedestal peak. Fig.10c shows the calibration spectrum using the  $\text{Cd}^{109}$  radioactive source. The resolution  $\sigma/\text{Peak}$  of the YAP detector is only  $\sim 26\%$  at 22 keV, which is expected due to the finite photoelectron statistics for this type of scintillator. This resolution is considerably worse compared to the gaseous wire tube detector. Taking into account the relatively poor resolution of the YAP detector, we conclude that the result of this measurement is consistent with the corresponding result from the wire tube detector in Fig. 9a. However, Fig.10a shows few events with energy up to 20-25keV, which would indicate a presence of larger energies compared to what we measured with the gaseous wire tube detector in Fig.9 (at X-ray energy of  $\sim 20\text{keV}$  the gaseous detector has practically zero detection efficiency - see Fig.5a).

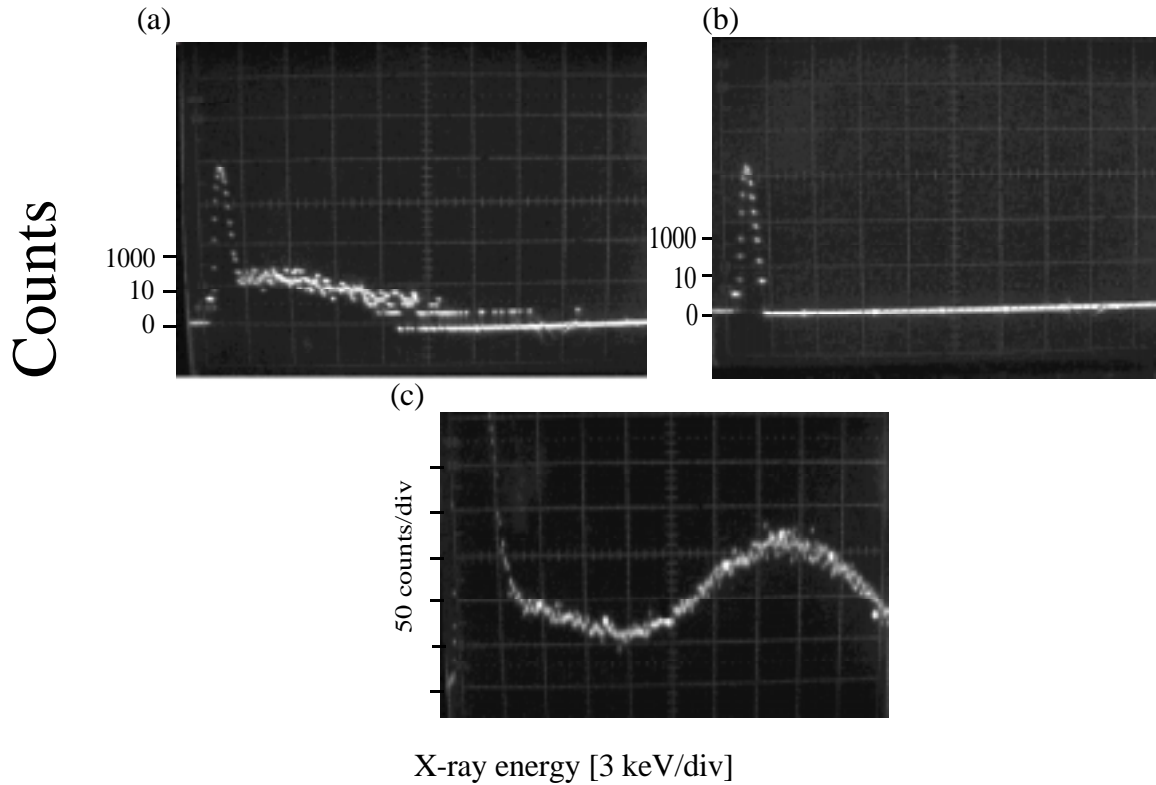


**Fig. 10.** (a) A measured X-ray pulse height spectrum using the YAP scintillation detector while sparking in xenon at  $\sim 1.81$  kV. The X-rays passing through the  $51 \mu\text{m}$  Mylar window in the sparking vessel, 3 cm of air, and a  $30 \mu\text{m}$  thick aluminized Mylar foil in the wire tube chamber (log vertical scale). (b) The same but the X-rays blocked with 1.5 mm thick lead sheet (log vertical scale). (c) The calibration with a  $\text{Cd}^{109}$  radioactive source producing 22 keV X-rays; the measured resolution  $\sigma/\text{Peak}$  is  $\sim 26\%$  at 22 keV (linear vertical scale). Every 50th count is bright.

### 3.4. X-ray production rate as a function of E/p, sparking voltage and gas

In this test, the X-rays pass through a  $51 \mu\text{m}$  thick Mylar window of the sparking vessel,  $\sim 3$  cm of air, and the Geiger detector window ( $38 \mu\text{m}$  thick Mylar), i.e., the X-rays below 2-3 keV were absorbed. We placed additional Mylar absorbers in front of the detector to evaluate the hardness of the X-ray radiation. The gases in the sparking vessel were hydrogen, air, nitrogen, argon, and xenon. We used the following gas pressure ranges:  $195\text{-}230 \mu$  for argon,  $120\text{-}140 \mu$  for xenon,  $280\text{-}320 \mu$  for air,  $275\text{-}330 \mu$  for nitrogen, and  $850\text{-}1020 \mu$  for hydrogen. Outside these pressure ranges the X-ray production stopped, although the spark gap continued to glow. Fig. 11 shows the measured X-ray rate in the Geiger detector as a function of the sparking voltage for several gases in

the sparking vessel. Notice that the argon X-ray spectrum appears to be hardest in this group of gases.

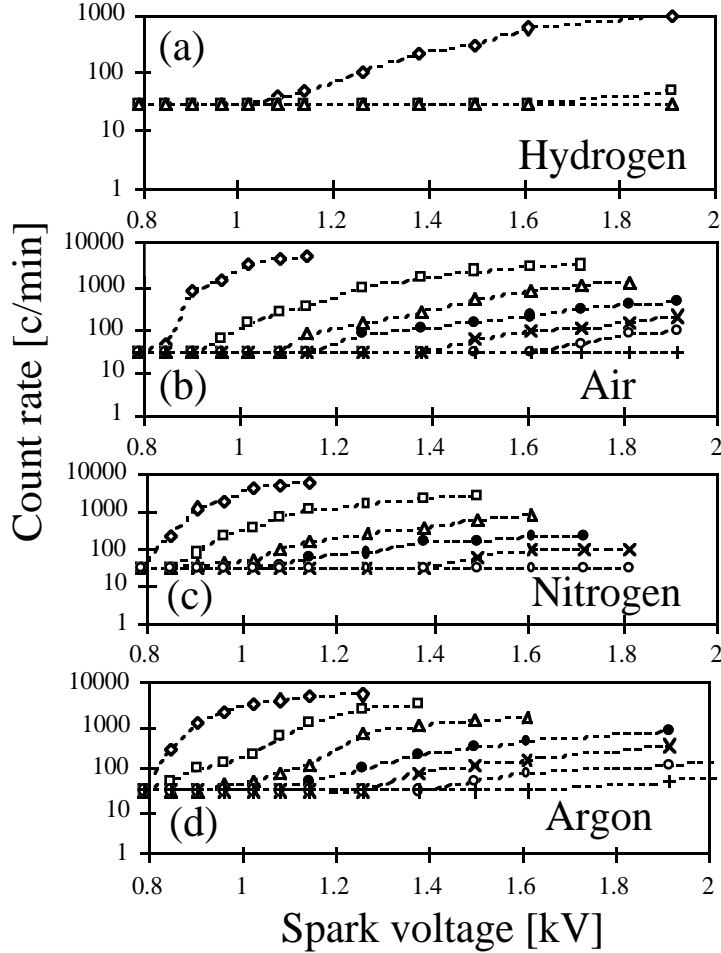


**Fig. 11.** The rate of the X-rays in the Geiger detector as a function of the sparking voltage  $V_{\text{spark}}$ , gas and a Mylar absorber thickness: for (a) hydrogen, (b) air, (c) nitrogen and (d) argon; no absorber (diamond) and Mylar absorbers of the following thickness: 127  $\mu\text{m}$  (square), 254  $\mu\text{m}$  (triangle), 356  $\mu\text{m}$  (filled circle), 483  $\mu\text{m}$  (x), 610  $\mu\text{m}$  (filled circles), and 711  $\mu\text{m}$  (cross).

Many gaseous phenomena depend on the  $E/N$  variable, where  $E$  is the electric field and  $N$  is the number of molecules per  $\text{cm}^3$ .  $E/N$  is often approximated by an  $E/p$  variable, where  $p$  is the gas pressure. For example, the electron drift velocity is often expressed as a function of  $E/p$ . Unfortunately, it is difficult to know  $E$  precisely due to a dynamic behavior of the spark; the space charge effects must also be very important for charges of  $\sim 10^{15}$  electrons per spark; for  $E/p$  higher than 10kV/cm/Torr, the electron energy is higher than  $\sim 50\text{eV}$ , causing ionization. Similarly, a

spark pressure may not be known since it depends on the spark temperature, which is not directly measured during the test (a surface temperature of the sparking vessel is increased rapidly; within 30 minutes it climbed to 70-80°C). Therefore, only approximations can be made. We assume that  $E = V_{\text{spark}}/d$ , where  $V_{\text{spark}}$  is determined from Fig.2c,  $d$  is  $\sim 1$  mm, and  $p$  is the gas pressure monitored  $\sim 20$ cm away from the sparking vessel.

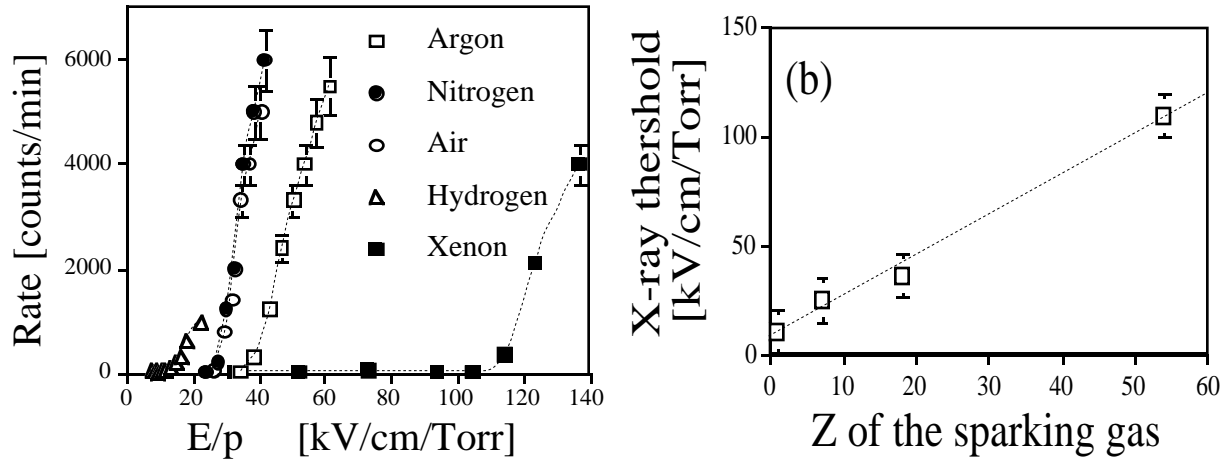


**Fig. 12.** (a) The production threshold and the rate dependence of the X-rays in the Geiger detector on the  $E/p$  value of the gas in the sparking vessel. (b) The dependence of the X-ray production threshold on the atomic number  $Z$  of the gas in the sparking vessel.

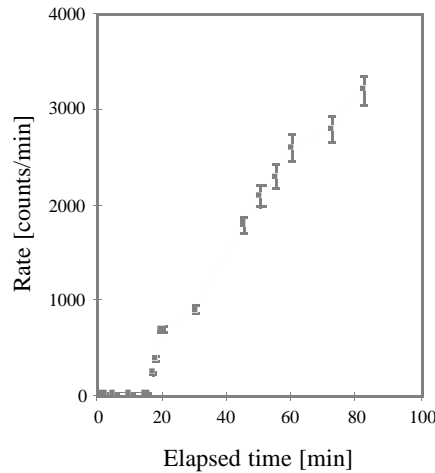


**Fig. 13.** The measured X-ray production rate as a function of elapsed time (sparking in air at  $V_{\text{spark}} \sim 0.9$  kV). The increase is due to the gas heating, which changes  $E/p$ .

Figure 12a shows the measured the X-ray rate in the Geiger detector as a function of the  $E/p$  value for several gases in the sparking vessel. In this measurement, no additional absorber was

placed between the sparking vessel and the detector. One can see that hydrogen starts producing the X-rays at the lowest  $E/p$ , xenon at highest. From Fig.12b it appears that the X-ray production threshold correlates with the atomic number  $Z$  of the gas.

Figure 13 shows the result in air at sparking voltage  $V_{\text{spark}} \sim 0.9\text{kV}$ . We see an increase in the rate as a function of elapsed time since the beginning of the sparking. This may be related to an increase in the sparking temperature which changes  $E/p$ .

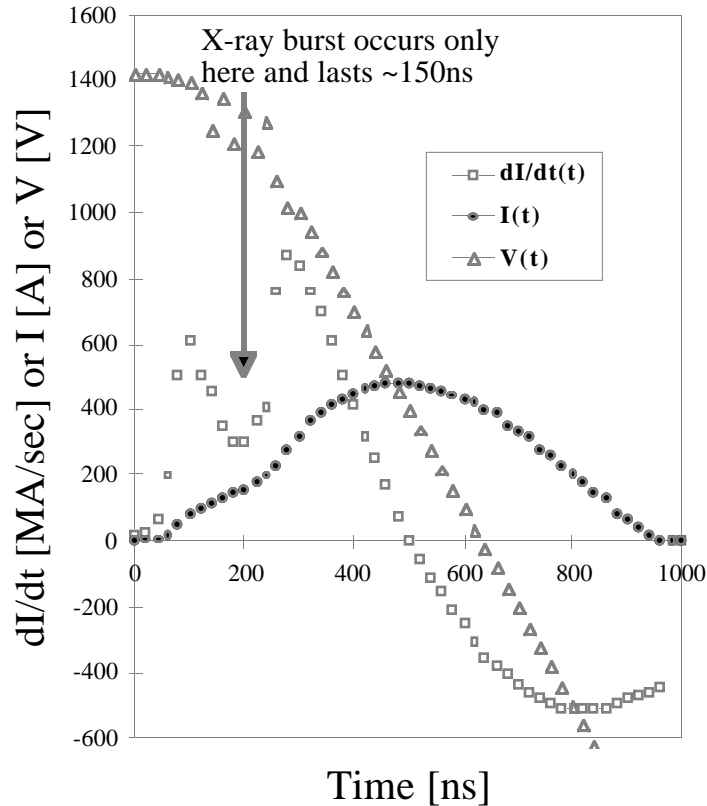


**Fig. 14.** Measured time development of the current  $I(t)$ , voltage  $V(t)$ , and current derivative  $dI/dt(t)$  relative to the X-ray production during our sparking tests. The X-ray burst duration is  $\sim 150\text{-}200\text{ns}$ , and is observed at  $\sim 200\text{ns}$  after the spark starts. The spark gap is operating, in this case, in air at  $V_{\text{spark}} \sim 1.4\text{kV}$  and  $p \sim 290 \mu$ ; similar shapes were measured at  $V_{\text{spark}} \sim 0.9\text{kV}$ .

### 3.5. The X-ray production and the $I$ , $V$ , and $dI/dt$ dependence of the spark

We have added several components to the setup of Fig.1 in order to measure the  $I(t)$ ,  $V(t)$ , and  $dI/dt(t)$  spark parameters. The current  $I(t)$  is measured with a  $1.2\Omega$  shunt resistor placed in the ground return of the spark gap, the voltage  $V(t)$  is measured with a simple 1000:1 divider, and the current derivative  $dI/dt(t)$  is measured using the toroid coil (so called Rogovski coil [7]). The coil is

placed around a conductor delivering the current into the spark gap; it has 30 turns, a minor radius of 4.2mm, and a major radius of ~17.8mm. To check the Rogovski coil measurement, we also performed a numerical derivative of the  $I(t)$  curve. Fig.14 shows time development of the current, voltage, and  $dI/dt$  during the spark and the relative timing of the X-ray production. The X-rays were measured in the wire tube or the YAP detectors.

We observe the first X-rays at ~200ns after the spark starts and are all contained within a time interval lasting 150-200ns, which corresponds to an observation of a slight dip in the current  $I(t)$ . The current dip also corresponds to the largest swing of the  $dI/dt(t)$ . The voltage measurement shows a small ripple effect at this time; however, we do not measure larger values than the expected spark voltage  $V_{\text{spark}}$ . The observation of the X-ray production during the dip in the current appears to be consistent with what has been observed during the pinch effect studies [1-4].

#### **4. DISCUSSION OF THE PRODUCTION MECHANISM OF THE X-RAYS**

We clearly see the production of soft X-rays with energies between 2 and 10keV, which are above the expected value given the known sparking voltage. The effect occurs during a slight dip in the current  $I(t)$ . This observation appears to be consistent with the earlier pinch effect studies [1-4], which are explained in the plasma field literature using the theory of radiation collapse [1].

However, one should stress that our spark energies at our smallest sparking voltage (~0.8kV) are at least a factor of  $\sim 4 \times 10^4$  smaller compared to the spark energies used in Refs.1-4. If our results are due to the pinch effect, we are then observing the pinch effect phenomenon at the smallest spark energy reported so far in the literature, i.e., we are investigating its threshold behavior. The maximum observed X-ray energy (~10keV), generated at the lowest voltage (~0.8kV), is ten times more than expected; it is above the K-shell energy for gases used in our tests, or the materials used in our spark electrodes (see Table 1 and Chapter 4). The X-ray production persists even for the carbon electrodes, which have the smallest K-shell energy (0.284keV); this would appear to eliminate the theory that the electrode atoms are responsible for the X-ray production. Furthermore, we have evidence that the production threshold and the X-ray rate is dependent on the gas choice in the sparking vessel. Because of the doubts that the pinch effect is the only explanation for the observed phenomenon, we were interested in searching for other possible explanations:

(a) The first obvious question is, if our spark voltages could produce the characteristic K-shell X-rays in the materials or gases which are present in our system, assuming a multi-electron participation on a liberation of a K-shell electron of some heavy atom such as iron, nickel, or molybdenum (see Table 1). The phenomenon would be similar to the multi-photon ionization of the gas impurities observed when a UV laser is shining into a gaseous drift chamber. However, it appears that such a production is very unlikely. It is difficult for a charged electron, having an

energy of only 50-100eV, to deeply penetrate inside the atom (compared to a neutral photon during the multi-photon excitation).

**Table 1** - Characteristic X-ray energies in keV of some elements which could exist in the vicinity of the spark, either in the gas or on the surface of the electrodes (a primary element or contamination); data obtained from the Handbook of Chemistry and Physics, published by the Chemical Rubber Co., Cleveland, Ohio, 1971, page E-178.

<b>Z</b>	<b>Element</b>	<b>K</b>	<b>L1</b>	<b>L2</b>	<b>L3</b>	<b>M1</b>	<b>N1</b>
6	Carbon	0.284					
7	Nitrogen	0.400					
8	Oxygen	0.532					
13	Aluminum	1.556	0.087	0.072			
14	Silicone	1.838	0.118	0.0077			
15	Phosphorus	2.142	0.153	0.128			
17	Chlorine	2.822	0.238	0.202	0.201	0.0297	
18	Argon	3.200	0.287	0.246	0.244	0.035	
20	Calcium	4.038	0.399	0.350	0.346	0.0471	
22	Titanium	4.966	0.530	0.462	0.456	0.0605	
24	Chromium	5.988	0.679	0.584	0.574	0.0762	
25	Manganese	6.542	0.762	0.656	0.644	0.0817	
26	Iron	7.113	0.849	0.722	0.709	0.0937	
28	Nickel	8.337	1.02	0.877	0.858	0.111	
40	Zirconium	17.998	2.533	2.308	2.224	0.432	0.0516
42	Molybdenum	20.003	2.869	2.630	2.525	0.509	0.0692
54	Xenon	34.551	5.448	5.103	4.783	1.14	0.208

To eliminate this possibility experimentally, we decided to use the carbon electrodes in the spark gap. The insulator is made of nylon to eliminate the porcelain,<sup>5</sup> which could in principle contain some ferro-electric crystals. We repeated the production of the soft X-rays with this setup under similar experimental conditions, as has been discussed in this paper. This indicates that the soft X-

<sup>5</sup> According to Dr. B. Manning of Champion Co., the porcelain in their spark plug (J-12Y) does not contain the ferro-electric crystals. The spark plug electrodes are made of Ni, Cr, Ma, Si, Ti, Zi alloy and traces of C and Fe; the ceramic insulator is made of Al<sub>2</sub>O<sub>3</sub> (~90%), and the glass phase is made of clay containing Ti, Ca, Na, Fe, Zi, etc., impurities).

ray production is very likely related to the gaseous phenomenon and not to the spark gap material, or to the insulator properties.

(b) In principle, the hot plasma can excite the X-rays through the "thermal Bremsstrahlung" phenomenon, which is caused by the electron-ion collisions at extremely high temperatures. It is necessary to heat the plasma to temperatures between  $10^7$  and  $10^8$  °K to excite the X-ray spectra seen in Fig. 9b. We exclude this possibility in our experiment because the predominant radiation from the spark is in the visible spectrum, and therefore, the average temperatures are very likely below  $10^4$  °K.

(c) One also cannot exclude that there is new physics, which goes either in parallel to the theory of the pinch effect, is driven by it, or even drives it. Refs. 8-12 suggest that both relativistic Schroedinger and Dirac wave equations allow atoms to have additional energy levels (so called Deep Dirac levels or DDL levels, which correspond to electron orbits close to the nucleus). Indeed, if such atomic levels exist then the plasma environment of the spark may be an ideal place to excite such transitions, because of a large number of ions and energetic electrons involved. A free energetic electron, perhaps even driven by the pinch effect, may enter an ion with such a velocity that it is captured by the new DDL atomic energy level. During such entry to the DDL level, the electron will radiate the Bremsstrahlung spectrum involving many photons, some of them would be X-rays (for example, the total energy released for hydrogen is close to  $\sim 509$ keV). One should mention that we have not observed any peaks in the X-ray energy distributions.

So far, we have not established proof that the DDL atoms exist. However, we continue this search and have finished building a larger detector capable of detecting soft X-rays over a larger solid angle. The aim of this search is two-fold: (a) to verify that the X-ray production is indeed isotropic, which must be an essential characteristic of the DDL atomic transitions (as opposed to the pinch effect), (b) to make a better estimate of the total energy sum per single event.

One may apply the results of this work to explain the soft X-ray spectra from various stars. For example, Fig. 15a shows a recent astronomical data of the X-ray flux originating from an object called PKS2155-304 as measured by the BeppoSAX satellite, equipped with the soft X-ray detectors [13]. Fig.15b shows the background spectrum from the Crab Nebula, which is used for normalization. Ref.13 speculates that the origin of these spectra is the Synchrotron emission. However, it is possible to explain, at least in principle, that the shape of the spectrum showed in Fig.15a is made of a composition of spectra similar to those shown in Fig. 9b from many contributing elements, i.e., using the plasma processes similar to those investigated by this work, as the origin of the soft X-rays from these objects.

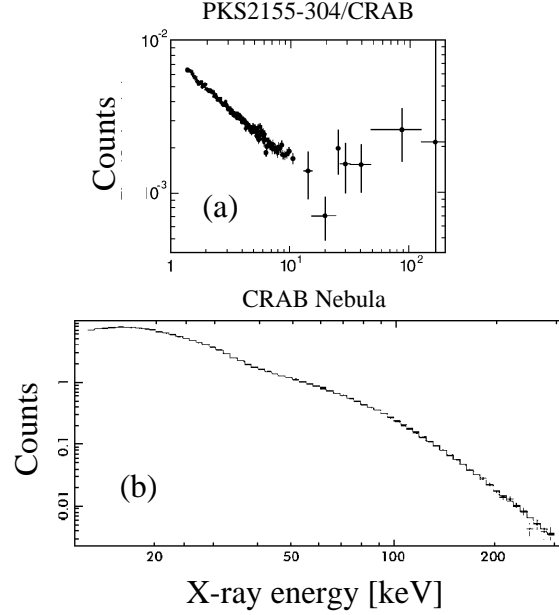


**Fig. 15.** (a) The recent astronomical data of the X-ray flux originating from an object called PKS2155-304 as measured by the BeppoSAX satellite, equipped with the soft X-ray detectors [8]; (b) the same for the CRAB Nebula, which is used for the normalization purpose in (a).

## CONCLUSIONS

1. We observe the production of soft X-rays of energy 2-10keV by sparking in hydrogen, air, nitrogen, argon, and xenon gases at low pressure with a sparking voltage as low as 0.8-1.6kV.
2. The X-ray events appear to come in clusters, with an average mean multiplicity of 3 per event into the solid angle of our long drift detector. The extrapolated production into a  $4\pi$ -solid angle is more than  $\sim 1500$  pulses, assuming the isotropic distribution.
3. The X-ray pulse height spectra in all tested gases have similar shapes resembling a power law distribution between 2 and 10 keV. Using the range method, the average measured X-ray energy is about 4keV.
4. The X-ray production threshold depends on E/p of the spark chamber gas. The threshold value increases as the gas Z increases.
5. The X-ray production persists even for the carbon electrodes; this would appear to eliminate the theory that electrode atoms are responsible for X-ray production.
6. We calculate that the probability to produce an X-ray event per one electron in a given spark is less than  $\sim 5 \times 10^{-16}$ . To observe this phenomenon, one needs very large currents. One would not see it with electrons from an ordinary  $\beta$ -source.
7. The paper also suggest that the observed X-rays could originate, at least partially, from a new

process, where energetic free electrons enter ions, and are captured on the DDL levels [8-12], radiating the Bremsstrahlung spectrum involving many photons.

8. If our results are due to the pinch effect, we are then observing the pinch effect phenomenon at the smallest spark energy reported so far in the literature, i.e., we are investigating its threshold behavior.

## ACKNOWLEDGMENTS

We are grateful to Catherine Maly for editing this paper. We would like to thank Dr. S. Majewski for providing the YAP scintillator for this test.

## REFERENCES

- [1] K.N. Koshelev and N.R. Pereira, *J. Appl. Phys.*, 69(1991)R21.
- [2] L. Cohen et al., *J. of the Optical Soc. of America*, 58(1968)843.
- [3] E.D. Korop et al., *Sov. Phys. Usp.* 22(1979)727, page 729.
- [4] G. Herziger et al., *Phys. Lett.*, A64(1978)390.
- [5] H. Pruchova and B. Franek, *Nucl. Instr & Meth.*, A366(1995)385; Issue of ICFA Instrumentation Bulletin, SLAC-PUB-7376, 1997; and H. Pruchova's Ph.D. thesis, Prague Tech. Univ.
- [6] E. Storm and H.I. Israel, "Photon cross-section from 1keV to 100MeV for Elements Z=1 to Z=100," *Atomic Data and Nucl. Data Tables* 7(1970)565.
- [7] For description of the Rogovski coil see for example S. Glasstone and R.H. Lovberg, "Controlled Thermonuclear Reactions," 1960, D. Van Nostrand Co., Inc., page 164.
- [8] J. A. Maly, J. Va'vra, "Electron Transitions on Deep Dirac Levels I," *Fusion Technology* 24, 307, (1993).
- [9] J. A. Maly, J. Va'vra, "Electron Transitions on Deep Dirac Levels II," *Fusion Technology* 27, 59, (1995).
- [10] J. A. Maly, J. Va'vra, "Electron Transitions on Deep Dirac Levels III. Electron densities in hydrogen-like atoms using the relativistic Schroedinger equation," Submitted to *Fusion Technology*, November 2, 1994.
- [11] J. A. Maly, J. Va'vra, "Electron Transitions on Deep Dirac Levels IV. Electron densities in the DDL atoms," Submitted to *Fusion Technology*, September 11, 1995.
- [12] J. A. Maly, J. Va'vra, "Electron Transitions on Deep Dirac Levels V. Negative energies in Dirac equation solutions give double deep Dirac levels (DDDL)," Submitted to *Fusion Technology*, February 8, 1996.
- [13] F. Frontera et al., *Proceedings of Compton GRO Symposium, Williamsburg, 1993*;  
P. Giommi et al., *Astronomy and Astrophysics*, May 28, 1997.